Anisotropic spin-orbit torque generation in epitaxial $SrIrO_3$ by symmetry design

T. Nan[a,1], T. J. Anderson[a,1], J. Gibbons[b], K. Hwang[c], N. Campbell[d], H. Zhou[e], Y. Q. Dong[e], G. Y. Kim[f], D. F. Shao[g], T. R. Paudel[g], N. Reynolds[b], X. J. Wang[h], N. X. Sun[h], E. Y. Tsymbal[g], S. Y. Choi[f], M. S. Rzchowski[d], Yong Baek Kim[c,i,j], D. C. Ralph[b,k] and C. B. Eom[a,2]

[a]Department of Materials Science and Engineering, University of Wisconsin-Madison, Madison, Wisconsin 53706, USA; [b]Laboratory of Atomic and Solid State Physics, Cornell University, Ithaca, New York 14853, USA; [c]Department of Physics and Centre for Quantum Materials, University of Toronto, Toronto, Ontario M5S 1A7, Canada; [d]Department of Physics, University of Wisconsin-Madison, Madison, Wisconsin 53706, USA; [e]Advanced Photon Source, Argonne National Laboratory, Argonne, Illinois 60439, USA; [f]Department of Materials Science and Engineering, POSTECH, Pohang 37673, Korea; [g]Department of Physics and Astronomy & Nebraska Center for Materials and Nanoscience, University of Nebraska, Lincoln, NE 68588, USA; [h]Department of Electrical and Computer Engineering, Northeastern University, Boston, Massachusetts 02115, USA; [i]Canadian Institute for Advanced Research/Quantum Materials Program, Toronto, Ontario M5G 1Z8, Canada; [j]School of Physics, Korea Institute for Advanced Study, Seoul 130-722, Korea; and [k]Kavli Institute at Cornell for Nanoscale Science, Ithaca, New York 14853, USA

Abstract:

Spin-orbit coupling (SOC), the interaction between the electron spin and the orbital angular momentum, can unlock rich phenomena at interfaces, in particular interconverting spin and charge currents. Conventional heavy metals have been extensively explored due to their strong SOC of conduction electrons. However, spin-orbit effects in classes of materials such as epitaxial 5*d*-electron transition metal complex oxides, which also host strong SOC, remain largely unreported. In addition to strong SOC, these complex oxides can also provide the additional tuning knob of epitaxy to control the electronic structure and the engineering of spin-to-charge conversion by crystalline symmetry. Here, we demonstrate room-temperature generation of spin-orbit torque on a ferromagnet with extremely high efficiency via the spin-Hall effect in epitaxial metastable perovskite $SrIrO_3$. We first predict a large intrinsic spin-Hall conductivity in orthorhombic bulk $SrIrO_3$ arising from the Berry curvature in the electronic band structure. By manipulating the intricate interplay between SOC and crystalline symmetry, we control the spin-Hall torque ratio by engineering the tilt of the corner-sharing oxygen octahedra in perovskite $SrIrO_3$ through epitaxial strain. This allows the presence of an anisotropic spin-Hall effect due to a characteristic structural anisotropy in $SrIrO_3$ with orthorhombic symmetry. Our experimental findings demonstrate the heteroepitaxial symmetry design approach to engineer spin-orbit effects. We therefore anticipate that these epitaxial 5*d* transition-metal oxide thin films can be an ideal building block for low-power spintronics.

spin-Hall effect | spin-orbit torque | complex oxides | strong spin-orbit coupling

Author Contributions: T.N., T.J.A. and C.B.E. conceived the research. C.B.E., D.C.R, Y.B.K., M.S.R., S.Y.C. and N.X.S. supervised the experiments. T.J.A. and T. N. performed the sample growth and surface/structural characterizations. T.N. performed the device fabrication. T.N., J.G, and D.C.R performed ST-FMR measurements and analysis. N.R., J.G. and D.C.R performed MOKE measurements. J.G., D.C.R., W.X.J. and N.X.S. performed magnetic characterizations. N.C., T.N., T.J.A. and M.S.R. carried out the electrical transport measurements. K.H. and Y.B.K. performed the tight-binding model calculations. D.F.S., T.R.P and E.Y.T performed the first principles calculations. G.Y.K. and S.Y.C. carried out the high-resolution TEM experiments. H.Z. and Y.D. carried out the synchrotron diffraction measurements. T.N., T.J.A., K.H. and C.B.E. wrote the manuscript. All authors discussed the results and commented on the manuscript. C.B.E. directed the research.
The authors declare no conflict of interest.

[1]T.N. and T.J.A. contributed equally to this work.
[2]To whom correspondence may be addressed. Email:ceom@wisc.edu

Current-induced spin-torque originating from spin-orbit effects offers an energy-efficient scheme for the electrical manipulation of magnetic devices(1–4). A large spin-torque efficiency, arising from either the spin-Hall effect(5–7) or the Rashba-Edelstein effect(8), is highly-desirable for enabling broad applications in spintronics. Great effort has been focused therein on semiconductors(9, 10), heavy metals(11–18), oxides(19, 20), and, more recently, topological insulators with a spin-momentum locked surface state(21–24). In the case of 5*d*-electron transition metal oxides, the delicate interplay between strong spin-orbit coupling and electron-electron correlation is believed to lead to non-trivial quantum phases(25–30), e.g., topological semimetals(31), quantum spin-Hall materials(32), and topological Mott insulators(27). The interplay between crystal structure and strong spin-orbit coupling (SOC) of conduction electrons can produce a large Berry curvature that gives rise to an intrinsic spin-Hall effect(33). Furthermore, due to the sensitive dependence of the electronic structure on crystalline symmetry, the efficiency of the spin/charge current conversion can be possibly modulated through heteroepitaxy. However, such material systems remain largely unexplored in the field of spin-orbitronics.

We first motivate our work with theoretical calculations that show a large intrinsic spin-Hall effect in the orthorhombic bulk semimetal $SrIrO_3$ (Fig. 1A). Large spin-Hall conductivity [SHC $\sim 2\times10^4$ $(\hbar/2e)(\Omega\ m)^{-1}$] is obtained over the extended region around the Fermi energy including the charge neutral point from the linear response theory for the bulk orthorhombic perovskite structure (Fig. 1C). The spin-Hall effect arises due to the Berry curvature of the electronic band structure, mainly from the nearly degenerate energy bands (Fig. 1B). The momentum-resolved SHC (see *SI Appendix* for details) revealed that the high intensities of SHC appear around the *k* points where the Fermi level crosses the nearly degenerate bands. Such a characteristic band structure is unique and occurs as a combined effect of SOC and the IrO_6 octahedral tilting/rotation in the bulk system, which is closely related to the non-symmorphic symmetry of the bulk crystal structure(34, 35). Due to the extended nature of the $SrIrO_3$ 5*d* orbitals, the electronic structure of $SrIrO_3$ is sensitive to changes in lattice symmetry. We reiterate that the large spin-Hall effect occurs only when the film has the orthorhombic structure due to its origins from the underlying bulk band structure. This suggests a new approach to engineer the spin-Hall effect by precise control of oxygen octahedral tilting, which allows fine-tuning of the electronic band structure.

We illustrate our crystalline symmetry design principles for engineering a large spin-Hall effect in Fig. 1D, in which the $SrIrO_3$ crystalline symmetry is manipulated by utilizing a lattice symmetry-mismatched $SrIrO_3/SrTiO_3$ heterointerface and atomic layer-by-layer control of the $SrIrO_3$ layer thickness. The crystalline symmetry of perovskite oxides is directly related to the connectivity of corner-sharing octahedra that can be manipulated by epitaxial strains or interfacial couplings(36). In the case of $SrIrO_3$ films near the $SrIrO_3/SrTiO_3$ interface, the IrO_6 octahedral tilting follows the non-tilted $SrTiO_3$ substrate due to the structure imprint of the cubic symmetry of $SrTiO_3$. Such a nearly complete suppression of IrO_6 octahedral tilting in ultrathin $SrIrO_3$ films gives rise to a tetragonal symmetry, whereas the degree of tilting in increasingly thicker films approaches that of bulk $SrIrO_3$. Experimentally, our synchrotron x-ray diffraction of variable thickness films directly confirmed such a structural symmetry transition in $SrIrO_3$, while our measurements of the spin-Hall effect in $SrIrO_3$ showed an enhancement, coincident with this transition to orthorhombic symmetry. We also observed a large anisotropy in the spin-Hall effect enabled by the structural anisotropy of the orthorhombic state. These results demonstrate that oxide perovskites not only possess a large spin-Hall effect at room temperature, but also enables further tuning of spin-orbit effects by symmetry design.

Epitaxial $SrIrO_3$ thin films were grown on (001) $SrTiO_3$ substrates by pulsed laser deposition with *in situ* high-pressure RHEED (see *SI Appendix* for details). Ferromagnetic Permalloy $Ni_{81}Fe_{19}$ (Py) polycrystalline thin films were then sputtered *in situ* on $SrIrO_3$, preserving critical interface transparency

for spin-current transmission and efficient spin-orbit torque (SOT) generation(37, 38). A 1 nm Al_2O_3 layer was added to prevent oxidation of Py. A control sample with an *ex situ* Py/$SrIrO_3$ interface showed a 4 times smaller efficiency for spin-torque generation due to the reduced spin current transmissivity at the interface. Atomic force microscopy images of the 1 nm Al_2O_3/3.5 nm Py/8 nm (20 unit cell) $SrIrO_3$ surface reveal an atomically-smooth surface (see *SI Appendix* for details). In Fig. 2, we show the cross-sectional filtered STEM-HAADF image of a 20 unit cell (uc) $SrIrO_3$ film on (001) $SrTiO_3$ capped with 2.5 nm Py. From the image, we determined that the high-quality $SrIrO_3$ film shares the same pseudocubic epitaxial arrangement as the $SrTiO_3$ substrate, with sharp interfaces between both $SrTiO_3$/$SrIrO_3$ and $SrIrO_3$/Py with no evidence on the existence of oxidized Py at the interface (see *SI Appendix* for details). We confirmed by x-ray diffraction that the $SrIrO_3$ film grows along $[110]_o$ (subscript o for orthorhombic notation) out-of-plane, and with $[1\bar{1}0]_o$ and $[001]_o$ in-plane along the [100] and [010] directions of $SrTiO_3$, respectively (see *SI Appendix* for details). For simplicity, we use pseudocubic indices *a*, *b* and *c* to represent orthorhombic $[1\bar{1}0]_o$, $[001]_o$, and $[110]_o$ orientations, respectively.

The spin-Hall effect in $SrIrO_3$ was probed by measuring the spin-orbit torque produced in the adjacent Py layer with spin-torque ferromagnetic resonance (ST-FMR)(12, 21, 38), as illustrated in the schematics (Fig. 3A). When an alternating charge current flows in $SrIrO_3$, the spin-Hall effect induces a spin current that flows into Py. This spin current exerts torque on the Py and excites the magnetic moment into precession, generating an alternating change of the resistance due to the anisotropic magnetoresistance (AMR) in Py. We measure a dc voltage signal V_{mix} across the device bar that arises from the mixing between the alternating current and changes in the device resistance. The ST-FMR spectrum can be obtained by sweeping external in-plane magnetic fields through the Py resonance condition (see *SI Appendix* for details), from which the resonance lineshape has been used to evaluate the efficiency of the torque. This would require a precise calibration of the microwave current in the bilayer. However, we find that the impedance of the $SrTiO_3$ substrates decreases at microwave frequencies to become comparable to the bilayer, thus leading to microwave current shunting through substrates. This may affect the result based on ST-FMR lineshape analysis (see *Materials and Methods* for details).

We evaluated the spin-torque ratio, which describes the efficiency of in-plane component of torque $\tau_\parallel$ generation relative to the charge current density in $SrIrO_3$ via spin-Hall effect ($\theta_\parallel=(\hbar/2e)j_S/j_C$, where j_S is the spin current density absorbed by the Py, and j_C is the applied charge current density in $SrIrO_3$), in $SrIrO_3$ by measuring the dc current-induced changes in of the ST-FMR lineshape (dc-tuned ST-FMR)(11, 12, 38). The injection of the dc current exerts an additional dc spin-torque on the adjacent Py, which modifies the Py resonance linewidth *W* (and effective Gilbert damping α_{eff}), as this torque component adds to or subtracts from the Gilbert damping torque depending on the relative orientation between the current and magnetic field(11). This linewidth modification due to the applied dc current should be unaffected by microwave frequency current shunting through $SrTiO_3$ substrates, and the anomalous Nernst effect in Py due to unintentional thermal gradients. A quantitative analysis of the spin-torque ratio $\theta_\parallel$ for 3.5 nm Py/8 nm (20 uc) $SrIrO_3$ bilayers is shown in Fig. 3B, where *W* and α_{eff} scale linearly with the applied dc current. The current is applied parallel to the *a*-axis and the in-plane magnetic field is swept at an angle φ =-45°, with respect to the current axis. The magnitude of the in-plane torque is proportional to the change of the effective Gilbert damping α_{eff} over the current density j_c in $SrIrO_3$. By averaging measurements at different frequencies (see *SI Appendix* for the frequency dependence of $\theta_\parallel$), we find that the spin-torque ratio, $\theta_\parallel$=0.51±0.07 for 3.5 nm Py/8 nm (20 uc) $SrIrO_3$, comparable to the highest values reported for heavy metal systems(7, 39), and 4 times as larger as that of a 4 nm Py/ 4 nm Pt control sample ($\theta_\parallel$=0.12±0.03). The sign for $\theta_\parallel$ is consistent with our first-principle calculations for bulk $SrIrO_3$ and experimental results on the heavy metal Pt. We examine the symmetry of the in-plane current-

induced torque by performing Py magnetization angular dependence dc-tuned ST-FMR. Fig. 3C shows the current-induced change in the effective damping $\Delta\alpha_{eff}/j_c$ (slope of the linear fit in Fig. 3B) as a function of in-plane magnetic field angle φ, which fits to $\sin\varphi$. This is consistent with the symmetry of the conventional current-induced torque that has been observed previous in polycrystalline heavy metal/ferromagnet bilayer systems(15).

As a comparison, a significantly smaller spin-torque ratio $\theta_{\parallel}$ was observed in the 3.5 nm Py/3.2 nm (8 uc) $SrIrO_3$ bilayer sample as shown in Fig. 3D where the current-induced change in the effective damping is smaller. We attribute the large difference of $\theta_{\parallel}$ in 8 uc and 20 uc $SrIrO_3$ samples to their structural transition with thickness (from tetragonal to orthorhombic) due to the structural imprint of non-tilted $SrTiO_3$ substrates as illustrated in Fig.1C. This agrees with our theory prediction of large spin-Hall effect in $SrIrO_3$ with an orthorhombic structure (the dependence of the spin-torque ratio on $SrIrO_3$ film thickness will be discussed next).

Interestingly, we also observed a significant dependence of the spin-torque ratio on crystallographic orientation in the thicker $SrIrO_3$ sample (3.5 nm Py/8 nm $SrIrO_3$) as shown in Fig. 3E (blue circle), where the $\theta_{\parallel}$ was extracted from devices with the charge current applied along various in-plane crystal orientations (from *a*- to *b*-axis) while keeping the magnetic field angle φ=-45°. Owing to the anisotropic structural characteristics of the orthorhombic symmetry, the IrO_6 octahedral rotation is out-of-phase along the *a*-axis (top-left of Fig. 3E), whereas it is in-phase along the *b*-axis (top-right of Fig. 3E), which gives rise to a different oxygen octahedral configuration when the charge current is applied along the *a*- or *b*-axis, and, therefore, the anisotropic $\theta_{\parallel}$. This contrasts the nearly isotropic $\theta_{\parallel}$ observed in the thinner $SrIrO_3$ sample (3.5 nm Py/8 nm $SrIrO_3$, red square), which was found to exhibit almost total suppression of the octahedral tilt along both the *a*- and *b*-axes (bottom of Fig. 3E) compared to the thicker film (Supplmentary Information). Such dependence on crystallographic orientation of the spin-torque ratio in tetragonal and orthorhombic $SrIrO_3$ demonstrates the strong correlation between the spin-Hall effect and the crystalline symmetry.

The dependence of the spin-torque ratio on the thickness of the $SrIrO_3$ layer and on the direction of current relative to the crystal axes was also confirmed by another independent characterization technique, in which the spin-torque-induced magnetization rotation in Py was measured by the polar magneto-optic-Kerr-effect (MOKE)(40). In a 5.5 nm Py/10 nm $SrIrO_3$ sample with the current applied along *a*-axis, the spin-torque ratio was measured to be 0.15±0.01, which is 2-3 times as large as a Py/Pt control sample measured by the MOKE (0.065±0.01, see *SI Appendix* for details). This is qualitatively consistent with our dc-tuned ST-FMR results, although the absolute value of the spin-torque ratio is smaller. Nevertheless, the MOKE measurements confirm the large lattice symmetry dependence ($\theta_{\parallel}$=0.15±0.01 in the 25 uc $SrIrO_3$ sample, while 0.013±0.01 in the 8 uc $SrIrO_3$ sample) and the anisotropic spin-torque ratio ($\theta_{\parallel}$=0.15±0.01 with $j_c \| a$-axis, while 0.05±0.005 with $j_c \| b$-axis in the 25 uc $SrIrO_3$ sample), which are qualitatively consistent with the trends obtained in our dc-tuned ST-FMR measurements.

To analyze the effect of lattice symmetry on spin-Hall effect in detail, we studied the dependence of the spin-torque ratio on varying thicknesses of $SrIrO_3$ films. From synchrotron x-ray measurements, we robustly established the previously-discussed suppression of IrO_6 octahedral tilt for ultrathin $SrIrO_3$ films, which modifies the symmetry of $SrIrO_3$ from orthorhombic to tetragonal (see *SI Appendix* for details)(41–43). As shown in Fig. 4A, this transition is characterized by the orthorhombicity factor defined as a_o/b_o (orthorhombic indices), which illustrates a tetragonal-to-orthorhombic $SrIrO_3$ structural transition around 4.8 nm (12 uc). We then measured the spin-torque ratio on the same series of $SrIrO_3$/Py bilayer samples (with fixed Py thickness). Accordingly, as shown in Fig. 4B, $\theta_{\parallel}$ increases sharply and saturates at the

thickness of 6.4 nm (16 uc) from a nearly constant value when the thickness is below 10 uc. The spin-torque ratio is also expected to increase and saturate when the thickness of the spin-Hall source material exceeds the spin diffusion length based on the standard spin diffusion theory(44). However, the abrupt change of $\theta_{\|}$ occurs at the $SrIrO_3$ structural transition thickness, which cannot be explained simply by the diffusive spin transport, as we determined a short spin diffusion length of ~1.4 nm (3.5 uc) for tetragonal $SrIrO_3$ from the thickness dependence of the over-layer Py Gilbert damping enhancement (Fig. 4C, see *Materials and Methods* for the estimation of spin diffusion length, spin mixing conductance and intrinsic spin-Hall angle). This strong dependence of $\theta_{\|}$ on lattice symmetry rather than on spin diffusion illustrates a direct connection between the degree of IrO_6 octahedral tilt and the spin-torque efficiency.

To gain more insight into the crystalline symmetry dependence of spin-Hall effect, we performed additional SHC calculations on tetragonal and orthorhombic phases of $SrIrO_3$ with density functional theory (DFT) calculated band structures (see *SI Appendix* for details). Qualitatively consistent with our experimental results, the orthorhombic phase of $SrIrO_3$ shows a larger SHC, which can be attributed to its narrow t_{2g} bands with more band crossings protected by symmetry, which is determined by the IrO_6 octahedral tilting.

In summary, we have proposed and developed a new material for spin-orbit torque applications in a transition metal perovskite with spin-orbit coupled 5*d* electrons, in which the interplay between SOC and the crystal structure produces a large spin-torque ratio. Furthermore, the extended nature of *5d* orbitals allows a sensitive response of the electronic band structure to an externally manipulated lattice structure, as manifested in the strong dependency of the spin-Hall effect on the degree of IrO_6 octahedral tilting in epitaxially-strained $SrIrO_3$. Such intricate coupling between the electronic and lattice degrees of freedom can thus open up a new avenue to engineer spin-orbit effects by tailoring the lattice symmetry through heteroepitaxy. This material acts as an ideal building block for oxide spintronics, since a broad range of ferromagnetic perovskites can be integrated in an epitaxial heterostructure with atomically sharp interfaces for efficient spin-current transmission. Therefore, we anticipate that the use of 5*d* transition metal perovskites could lead to substantial advances in spintronics.

Materials and Methods

Sample growth, fabrication and characterization. $SrIrO_3$ films were epitaxially synthesized on (001) $SrTiO_3$ substrates using pulsed laser deposition (PLD). During the growth, layer-by-layer deposition was observed by *in situ* reflection high energy electron diffraction (RHEED). Before the growth, the $SrTiO_3$ (001) substrates were chemically etched and annealed to ensure TiO_2 surface termination. The substrates were first immersed in buffered hydrofluoric acid for 60 seconds before being annealed at 900 °C for 6 hours in an O_2-rich environment. After annealing, the substrates were etched again in buffered hydrofluoric acid to remove any leftover SrO on the surface. The PLD growth was conducted at a substrate temperature of 600 °C and an oxygen partial pressure of 75 mTorr. The laser fluence at the $SrIrO_3$ target surface was ~1 J/cm^2 and the pulse repetition was 10 Hz. The working distance between target and substrate was ~58 mm. After the $SrIrO_3$ growth, the sample was cooled down in an oxygen rich atmosphere. The chamber was re-evacuated at room temperature and Py was sputter deposited at an Ar pressure of 3 mTorr with a background pressure $<2\times10^{-8}$ Torr, followed by a 1 nm Al passivation layer. The Py film is shown to be polycrystalline, which we confirmed by the observation of RHEED diffraction rings after deposition. The atomically flat Py surface on top of $SrIrO_3$ was verified using atomic force microscopy (see *SI Appendix* for details). We confirmed the thickness, epitaxial arrangement, and coherence of the $SrIrO_3$ films using x-ray reflectivity, x-ray diffraction, and reciprocal space mappings (see *SI Appendix* for details). The coherent $SrIrO_3$ films assembled on the cubic $SrTiO_3$ substrate with the

orthorhombic $SrIrO_3$ $[1\text{-}10]_o$, $[001]_o$, and $[110]_o$ directions along the cubic $SrTiO_3$ [100], [010], and [001] directions, respectively, and the misfit epitaxial strain from the $SrTiO_3$ induced a monoclinic distortion of the $SrIrO_3$ unit cell, which is consistent with similar orthorhombic perovskites grown on cubic substrates (see *SI Appendix* for details)(45). The thickness of Py films was measured by using x-ray reflectivity.

We patterned the Py/$SrIrO_3$ sample by using photolithography followed by ion beam milling. Then 200 nm Pt/5 nm Ti electrodes were sputter deposited and defined by a lift-off procedure. Devices for ST-FMR were patterned into microstrips (20-50 μm wide and 40-100 μm long) with ground-signal-ground electrodes. Devices for electrical transport measurements were patterned into 100 μm wide and 500 μm long Hall bars.

STEM measurements. TEM specimens were prepared by a focused ion multi-beam system (JIB-4610F, JEOL, Japan). To protect the Py/$SrIrO_3$ films, an amorphous carbon layer was deposited on the top surface before the ion beam milling. A Ga^+ ion beam with an acceleration voltage of 30 kV was used to fabricate the thin TEM lamella. To minimize the surface damage induced by the Ga^+ ion beam milling, the sample was further milled by an Ar^+ ion beam (PIPS II, Gatan, USA) with an acceleration voltage of 100 V for 4 minutes. HAADF-STEM images were taken by using a scanning transmission electron microscope (JEM-2100F, JEOL, Japan) at 200 kV with a spherical aberration corrector (CEOS GmbH, Germany). The optimum size of the electron probe was ~0.9 Å. The collection semi-angles of the HAADF detector were adjusted from 70 to 200 mrad in order to collect large-angle elastic scattering electrons for clear *Z*-sensitive images. The obtained raw images were processed with a band-pass Wiener filter with a local window to reduce a background noise (HREM research Inc., Japan).

ST-FMR measurements. During ST-FMR measurements, a microwave current at a fixed frequency (4.5 to 7 GHz) is applied through the ac port of a bias-T to a RF ground-signal-ground probe tip. The microwave power output (8 to 14 dBm) is also fixed. The in-plane magnetic fields are generated by a rotary electromagnet which allows for magnetic field angle dependence of ST-FMR measurements. Magnetic fields are swept from 0-0.12 T for driving the Py through its resonance condition. The resonance line shape can be fitted to a sum of symmetric and antisymmetric Lorentzian components, where the anti-damping (in-plane, $\tau_\parallel$) and field-like torque (out-of-plane, $\tau_\perp$) components are proportional to the amplitudes of the symmetric and antisymmetric line shape, respectively. By performing the lineshape analysis, the spin-torque ratio can be determined. However, we find through RF transmission measurements that although bare $SrTiO_3$ is nonconductive at low frequencies, after processing, it has a finite impedance at microwave frequencies, and as a consequence RF current is shunted through the $SrTiO_3$ substrate during ST-FMR measurements. This shunting may cause potential additional contributions to the Oersted field and modify the size of the antisymmetric component of the lineshape. Additionally, the unknown current shunted through the $SrTiO_3$ poses a challenge for determining the RF current flowing through our $SrIrO_3$ layer based on RF transmission calibration. Hence, it is difficult to determine the size of the spin-Hall effect in $SrIrO_3$ from RF lineshape analysis alone. For this reason, we rely on dc-tuned ST-FMR measurements, for which the linewidth modification due to the applied DC current should be unaffected by microwave frequency current shunting, and polar magneto-optic Kerr effect (MOKE) measurements, for which RF current is unnecessary. Both of these measurement methods should be unaffected by the high-frequency conductivity of the $SrTiO_3$ substrate.

In dc-tuned ST-FMR, we modulate the rf current amplitude and measure the mixing voltage signal by using a lock-in amplifier through the dc port of the bias-T. The modulation frequency is 437 Hz. The resonance line shape is fitted to a sum of symmetric and antisymmetric Lorentzian components, from which the resonance linewidth is extracted. We quantify the $\theta_\parallel$ by linear fitting the current dependent resonance linewidth or α_{eff} as $\left|\theta_\parallel\right| = \frac{2|e|}{\hbar}\frac{(H_{FMR}+M_{eff}/2)\mu_0 M_s t_{FM}}{|sin\varphi|}\left|\frac{\Delta\alpha_{eff}}{\Delta j_c}\right|$, where α_{eff} is the effective

magnetic damping of Py that is related to W as $\alpha_{eff} = \frac{\gamma}{2\pi f} W + W_0$ (W_0 is the inhomogeneous linewidth broadening); and γ, μ_0, M_{eff}, M_S, and t_{FM} are the gyromagnetic ratio, the permeability in vacuum, the effective magnetization, the saturation magnetization and the thickness of Py, respectively. We determined the Gilbert damping parameter and the effective magnetization by the frequency dependence of the resonance linewidth and the resonance field, respectively (see *SI Appendix*). The charge current density j_c is carefully calibrated by measuring the 4-point-resistance for each layer with a parallel resistor model (see *SI Appendix* for details).

MOKE measurements. Polar MOKE measurements of $\theta_{\parallel}$ were performed using a 630 nm diode laser, a Glan-Taylor polarizer with an extinction coefficient of 10^5:1, and a 10× infinity corrected microscope objective to focus 2 mW of optical power down to a 10 μm spot. An excitation current through the device of 7-10 mA at 5667 Hz was used to lock in to the response of the magnetization due to the anti-damping spin torque. The laser spot was scanned across the middle of the device at external fields of 0.08 T parallel and anti-parallel to the current flow direction in the device. The linear polarization incident on the sample was 45° rotated from the external field direction to suppress quadratic MOKE effects. $\theta_{\parallel}$ is quantified as by using the ratio of the integrated absolute value of the signal across the device that is even under the external magnetic field reversal (A_{sum}) and odd under magnetic field reversal (A_{diff}) according to $\theta_{||} = \frac{A_{diff}}{A_{sum}} \frac{e}{\hbar} \frac{\mu_0 M_S t_{FM} t_{tot} ln(4)}{X\pi}$ (see *SI Appendix* for details), where t_{tot} is the total thickness of the $SrIrO_3$/Py bilayer and X is fraction of current flowing through the $SrIrO_3$ as determined via the parallel resistor model described in the *SI Appendix*.

Synchrotron X-ray Thin Film diffraction. Synchrotron X-ray diffraction measurements were carried out to precisely characterize the structural and lattice symmetry evolution as a function of thickness of $SrIrO_3$ thin films epitaxially grown on a (001) $SrTiO_3$ substrate. The thin film diffraction measurements were performed on a five-circle diffractometer with χ-circle geometry, using an X-ray energy of 20 keV (wavelength λ = 0.6197 Å) at sector 12-ID-D of the Advanced Photon Source, Argonne National Laboratory. The X-ray beam at the beamline 12-ID-D has a total flux of 4.0×10^{12} photons/s and was vertically focused by beryllium compound refractive lenses down to a beam profile of ~ 50 μm. The L-scans along respective truncation rods {10L} were obtained by subtracting the diffuse background contributions using the two-dimensional images acquired with a pixel 2D array area detector (Dectris PILATUS-1mm Si 100K). The separation of respective {103} film peak positions in reciprocal space can be used to extract the out-of-plane tilt angle of the $SrIrO_3$ film with respect to the cubic $SrTiO_3$ lattice, so that we can obtain the degree of orthorhombic distortion (a/b> 1) for each $SrIrO_3$ thin film as a function of thickness (see *SI Appendix* for details).

Estimation of the spin diffusion length, spin mixing conductance and intrinsic spin-Hall angle in Py/$SrIrO_3$. To estimate the spin diffusion length in our $SrIrO_3$ thin film, we characterize the Gilbert damping parameter α of Py in Py/$SrIrO_3$ bilayers with various $SrIrO_3$ thicknesses by using both ST-FMR (on patterned samples) and broadband FMR measurements (on 5 mm by 5 mm samples). In broadband FMR measurements, the microwave magnetic field is produced by a coplanar waveguide, and the resonance spectrum is obtained by sweeping external magnetic fields through the Py resonance condition with a fixed microwave frequency. We measure the field derivative of the FMR absorption intensity with field modulation at low frequency (<1 kHz). In both techniques, we perform frequency dependent measurements, from which the resonance linewidth of Py is obtained at each frequency. The Gilbert damping parameter α is then calculated as $W = W_0 + \frac{2\pi\alpha}{|\gamma|} f$, where W_0 is the inhomogeneous linewidth broadening. We observed the enhancement of α with increasing $SrIrO_3$ thickness due to the spin pumping

effect as shown in Fig. 4C. The data can be fitted to a diffusive spin transport model as(46), $\alpha = \alpha_0 + \frac{g_{op}\mu_B\hbar}{2e^2M_s t_{SIO}}[\frac{1}{G_{\uparrow\downarrow}} + 2\rho(t)\lambda_s \coth(\frac{t}{\lambda_s})]^{-1}$, where g_{op} is the Lande g factor, α_0 is the Gilbert damping with zero $SrIrO_3$ thickness, $G_{\uparrow\downarrow}$ is the interfacial spin mixing conductance per unit area, t is the thickness of $SrIrO_3$, $\rho(t)$ is the thickness dependent resistivity of $SrIrO_3$ and λ_s is the spin diffusion length in $SrIrO_3$. In this fitting, we take into account the thickness dependence of the $SrIrO_3$ resistivity which increases in ultrathin films due to scattering mechanisms (see *SI Appendix* for details), which gives a spin-mixing conductance $G_{\uparrow\downarrow}$ of 1.8 $\times 10^{14}$ Ω^{-1} m^{-2} and a spin diffusion length of 1.4 nm. These are consistent with that reported in the $LaSrMnO_3/SrRuO_3$ system(47). The value of the spin diffusion length corresponds to the tetragonal phase of $SrIrO_3$, since the damping parameter is largely saturated already for thicknesses less than the point of transition to the orthogonal phase at 4.8 nm (12 uc).

The spin torque exerted on the Py originates from the spin current that is transmitted through the interface and absorbed by Py. Therefore, the measurement of the spin-torque ratio provides the lower bound of the intrinsic spin-Hall effect, in which the spin-torque ratio $\theta_{\|}$ can be expressed as $\theta_{||} \equiv T\theta_{SH}$, where T is the spin current transmissivity, θ_{SH} is the intrinsic spin-Hall angle. The reduction of the spin current through the interface can be either due to spin backflow (48, 49) or spin memory loss mechanisms associated with spin-dependent interfacial scattering. If spin backflow is dominant, then based on the drift-diffusion approximation for a $SrIrO_3$ layer thicker than the spin-diffusion length, one should have $T \equiv \frac{2G_{\uparrow\downarrow}}{2G_{\uparrow\downarrow}+\sigma/\lambda}$, where $G_{\uparrow\downarrow}$, σ and λ are the spin mixing conductance, conductivity and spin diffusion length of the $SrIrO_3$ respectively. For the 3.5 nm Py/8 nm $SrIrO_3$ sample, $G_{\uparrow\downarrow} = 1.8 \times 10^{14}\ \Omega^{-1}\mathrm{m}^{-2}$, $\lambda = 1.4$ nm, and $\sigma = 2.5 \times 10^5\ \Omega^{-1}\mathrm{m}^{-1}$. We then obtain T=0.67, and $\theta_{SH} = 0.76 \pm 0.1$. Spin memory loss would contribute an additional reduction in the spin transmissivity, leading to an even larger estimate for the intrinsic spin-Hall angle in $SrIrO_3$.

Theoretical calculations. For the spin-Hall conductivity calculations, we employed a j_{eff}=1/2 tight-binding model constructed for the orthorhombic perovskite bulk $SrIrO_3$(34, 35). The model incorporates various spin-dependent hopping channels for Ir electrons generated by oxygen octahedron tilting in the bulk structure. The model Hamiltonian H consists of four doubly degenerate electron bands on account of the four Ir sites in each unit cell.

$$H = \sum_{\boldsymbol{k}} \psi_{\boldsymbol{k}}^{\dagger} H_{\boldsymbol{k}} \psi_{\boldsymbol{k}}$$

Here, $\psi = (\psi_{1\uparrow}, \psi_{2\uparrow}, \psi_{3\uparrow}, \psi_{4\uparrow}, \psi_{1\downarrow}, \psi_{2\downarrow}, \psi_{3\downarrow}, \psi_{4\downarrow})^T$ are electron operators with the subscripts meaning the sub-lattice (1,2,3,4) and j_{eff}=1/2 pseudo-spin $(\uparrow, \downarrow)$. The explicit form of H_k and the values of the hopping parameters can be found in Refs. 24 and 25. The electron band structure of the model is displayed in Fig. 1B. Then, the SHC tensor $\sigma_{\mu\nu}^{\rho}$ is calculated by the Kubo formula(7, 50):

$$\sigma_{\mu\nu}^{\rho} = \sum_{\boldsymbol{k}} \Omega_{\mu\nu}^{\rho}(\boldsymbol{k})$$

where

$$\Omega_{\mu\nu}^{\rho}(\boldsymbol{k}) = \frac{2e\hbar}{V} \sum_{\epsilon_{\mathbf{nk}} < \epsilon_F < \epsilon_{\mathbf{mk}}} \mathrm{Im}[\frac{\langle \mathbf{mk}|\mathcal{J}_{\mu}^{\rho}|\mathbf{nk}\rangle\langle \mathbf{nk}|J_{\nu}|\mathbf{mk}\rangle}{(\epsilon_{\mathbf{mk}} - \epsilon_{\mathbf{nk}})^2}].$$

Here, $J_{\nu} (= \sum_{\boldsymbol{k}} \psi_{\boldsymbol{k}}^{\dagger} \frac{\partial H_{\mathbf{k}}}{\partial k_{\nu}} \psi_{\boldsymbol{k}})$ is charge current, and $\mathcal{J}_{\mu}^{\rho} (= \frac{1}{4}\{\sigma^{\rho}, J_{\mu}\})$ is spin current with the j_{eff}=1/2 spin represented by the Pauli matrix σ^{ρ}. In the above expression, V is the volume of the system, ϵ_F is the Fermi

level, and $|\mathrm{m}\mathbf{k}\rangle$ represents a Bloch state of H with energy $\epsilon_{\mathrm{m}\mathbf{k}}$. The momentum-resolved SHC represented by $\Omega^{\rho}_{\mu\nu}(\boldsymbol{k})$ enables us to trace the electron states responsible for the large spin-Hall effect. More details of the theoretical calculation of SHC in $SrIrO_3$ can be found in a recent theoretical paper(51) by 2 authors from the current work.

ACKNOWLEDGMENTS. We acknowledge E. Y. Tsymbal, P. J. Ryan, D. D. Fong, and J. Irwin for discussions, S. Emori for comments on the manuscript, and Y. J. Ma, D. T. Harris, L. Guo, and J. Schad for technical assistance with experiments. T. Nan acknowledges L. C. Sun for assistance in graphic design. This work was supported by the National Science Foundation under DMREF Grant No. DMR-1629270, AFOSR FA9550-15-1-0334 and AOARD FA2386-15-1-4046. Work at Northeastern University is funded by the NSF TANMS ERC Award 1160504. This research used resources of the Advanced Photon Source, a U.S. Department of Energy (DOE) Office of Science User Facility operated for the DOE Office of Science by Argonne National Laboratory under Contract No. DE-AC02-06CH11357. Work at Cornell was supported by the National Science Foundation (DMR-1708499) and Western Digital, and made use of the Cornell Center for Materials Research Shared Facilities which are supported by the NSF MRSEC program (DMR-1120296). K. Hwang and Y. B. Kim are supported by the NSERC of Canada, Canadian Institute for Advanced Research, and Center for Quantum Materials at the University of Toronto.

1. Brataas A, Kent AD, Ohno H (2012) Current-induced torques in magnetic materials. *Nat Mater* 11:372–381.

2. Jungwirth T, Marti X, Wadley P, Wunderlich J (2016) Antiferromagnetic spintronics. *Nat Nanotechnol* 11:231–241.

3. Otani Y, Shiraishi M, Oiwa A, Saitoh E, Murakami S (2017) Spin conversion on the nanoscale. *Nat Phys* 13:829–832.

4. Gambardella P, Miron IM (2011) Current-induced spin-orbit torques. *Philos Trans R Soc A Math Phys Eng Sci* 369:3175–3197.

5. Dyakonov MI, Perel VI (1971) Current-induced spin orientation of electrons in semiconductors. *Phys Lett A* 35:459–460.

6. Hirsch JE (1999) Spin Hall effect. *Phys Rev Lett* 83:1834–1837.

7. Sinova J, Valenzuela SO, Wunderlich J, Back CH, Jungwirth T (2015) Spin Hall effects. *Rev Mod Phys* 87:1213–1260.

8. Edelstein VM (1990) Spin polarization of conduction electrons induced by electric current in two-dimensional asymmetric electron systems. *Solid State Commun* 73:233–235.

9. Kato YK, Myers RC, Gossard AC, Awschalom DD (2004) Observation of the spin Hall effect in semiconductors. *Science* 306:1910–1913.

10. Brüne C, et al. (2010) Evidence for the ballistic intrinsic spin Hall effect in HgTe nanostructures. *Nat Phys* 6:448–454.

11. Ando K, et al. (2008) Electric manipulation of spin relaxation using the spin Hall effect. *Phys Rev Lett* 101:036601.

12. Liu L, Moriyama T, Ralph DC, Buhrman RA (2011) Spin-torque ferromagnetic resonance induced

by the spin Hall effect. *Phys Rev Lett* 106:036601.

13. Liu L, et al. (2012) Spin-torque switching with the giant spin Hall effect of tantalum. *Science* 336:555–558.

14. Kim J, et al. (2013) Layer thickness dependence of the current-induced effective field vector in Ta|CoFeB|MgO. *Nat Mater* 12:240–245.

15. Garello K, et al. (2013) Symmetry and magnitude of spin-orbit torques in ferromagnetic heterostructures. *Nat Nanotechnol* 8:587–593.

16. Emori S, Bauer U, Ahn S-M, Martinez E, Beach GSD (2013) Current-driven dynamics of chiral ferromagnetic domain walls. *Nat Mater* 12:611–616.

17. Fan X, et al. (2013) Observation of the nonlocal spin-orbital effective field. *Nat Commun* 4:1799.

18. Zhang W, et al. (2014) Spin Hall effects in metallic antiferromagnets. *Phys Rev Lett* 113:196602.

19. Fujiwara K, et al. (2013) 5d iridium oxide as a material for spin-current detection. *Nat Commun* 4:2893.

20. Lesne E, et al. (2016) Highly efficient and tunable spin-to-charge conversion through Rashba coupling at oxide interfaces. *Nat Mater* 15:1261–1266.

21. Mellnik AR, et al. (2014) Spin-transfer torque generated by a topological insulator. *Nature* 511:449–451.

22. Fan Y, et al. (2014) Magnetization switching through giant spin-orbit torque in a magnetically doped topological insulator heterostructure. *Nat Mater* 13:699–704.

23. Rojas-Sánchez JC, et al. (2016) Spin to charge conversion at room temperature by spin pumping into a new type of topological insulator: α-Sn films. *Phys Rev Lett* 116:096602.

24. Li CH, et al. (2014) Electrical detection of charge-current-induced spin polarization due to spin-momentum locking in Bi_2Se_3. *Nat Nanotechnol* 9:218–24.

25. Witczak-Krempa W, Chen G, Kim YB, Balents L (2014) Correlated quantum phenomena in the strong spin-orbit regime. *Annu Rev Condens Matter Phys* 5:57–82.

26. Fang C, Lu L, Liu J, Fu L (2016) Topological semimetals with helicoid surface states. *Nat Phys* 12:936–941.

27. Pesin D, Balents L (2010) Mott physics and band topology in materials with strong spin–orbit interaction. *Nat Phys* 6:376–381.

28. Kondo T, et al. (2015) Quadratic Fermi node in a 3D strongly correlated semimetal. *Nat Commun* 6:10042.

29. Matsuno J, et al. (2015) engineering a spin-orbital magnetic insulator by tailoring superlattices. *Phys Rev Lett* 114:247209.

30. Nie YF, et al. (2015) Interplay of spin-orbit interactions, dimensionality, and octahedral rotations in semimetallic $SrIrO_3$. *Phys Rev Lett* 114:016401.

31. Wan X, Turner AM, Vishwanath A, Savrasov SY (2011) Topological semimetal and Fermi-arc surface states in the electronic structure of pyrochlore iridates. *Phys Rev B* 83:205101.

32. Shitade A, et al. (2009) Quantum spin Hall effect in a transition metal oxide Na_2IrO_3. *Phys Rev*

Lett 102:256403.

33. Xiao D, Chang MC, Niu Q (2010) Berry phase effects on electronic properties. *Rev Mod Phys* 82:1959–2007.

34. Carter JM, Shankar VV, Zeb MA, Kee HY (2012) Semimetal and topological insulator in perovskite iridates. *Phys Rev B* 85:115105.

35. Chen Y, Lu Y-M, Kee H-Y (2015) Topological crystalline metal in orthorhombic perovskite iridates. *Nat Commun* 6:6593.

36. Hwang HY, et al. (2012) Emergent phenomena at oxide interfaces. *Nat Mater* 11:103–113.

37. Zhang W, Han W, Jiang X, Yang S-H, Parkin SSP (2015) Role of transparency of platinum–ferromagnet interfaces in determining the intrinsic magnitude of the spin Hall effect. *Nat Phys* 11:496–502.

38. Nan T, et al. (2015) Comparison of spin-orbit torques and spin pumping across NiFe/Pt and NiFe/Cu/Pt interfaces. *Phys Rev B* 91:214416.

39. Demasius K-U, et al. (2016) Enhanced spin–orbit torques by oxygen incorporation in tungsten films. *Nat Commun* 7:10644.

40. Fan X, et al. (2016) All-optical vector measurement of spin-orbit-induced torques using both polar and quadratic magneto-optic Kerr effects. *Appl Phys Lett* 109:122406.

41. Schütz P, et al. (2017) Dimensionality-driven metal-insulator transition in spin-orbit-coupled $SrIrO_3$. *Phys Rev Lett* 119: 256404.

42. Groenendijk DJ, et al. (2017) Spin-orbit semimetal $SrIrO_3$ in the two-dimensional limit. *Phys Rev Lett* 119: 256403.

43. Chang SH, et al. (2011) Thickness-dependent structural phase transition of strained $SrRuO_3$ ultrathin films: The role of octahedral tilt. *Phys Rev B* 84:104101.

44. Tserkovnyak Y, Brataas A, Bauer GEW, Halperin BI (2005) Nonlocal magnetization dynamics in ferromagnetic hybrid nanostructures. *Rev Mod Phys* 77:1375–1421.

45. Vailionis A, et al. (2011) Misfit strain accommodation in epitaxial ABO_3 perovskites: Lattice rotations and lattice modulations. *Phys Rev B* 83:064101.

46. Boone CT, Nembach HT, Shaw JM, Silva TJ (2013) Spin transport parameters in metallic multilayers determined by ferromagnetic resonance measurements of spin-pumping. *J Appl Phys* 113:153906.

47. Emori S, et al. (2016) Spin transport and dynamics in all-oxide perovskite $La_{2/3}Sr_{1/3}MnO_3/SrRuO_3$ bilayers probed by ferromagnetic resonance. *Phys Rev B* 94:224423.

48. Haney P, et al. (2013) Current induced torques and interfacial spin-orbit coupling: Semiclassical modeling. *Phys Rev B* 87:174411.

49. Pai C, et al. (2016) Dependence of the efficiency of spin Hall torque on the transparency of Pt/ferromagnetic layer interfaces. *Phys Rev B* 92: 064426.

50. Guo GY, Murakami S, Chen TW, Nagaosa N (2008) Intrinsic spin Hall effect in platinum: First-principles calculations. *Phys Rev Lett* 100:096401.

51. Patri AS, Hwang K, Lee H-W, Kim YB (2017) Theory of large intrinsic spin Hall effect in iridate

semimetals. *Sci Rep* 8:8052.

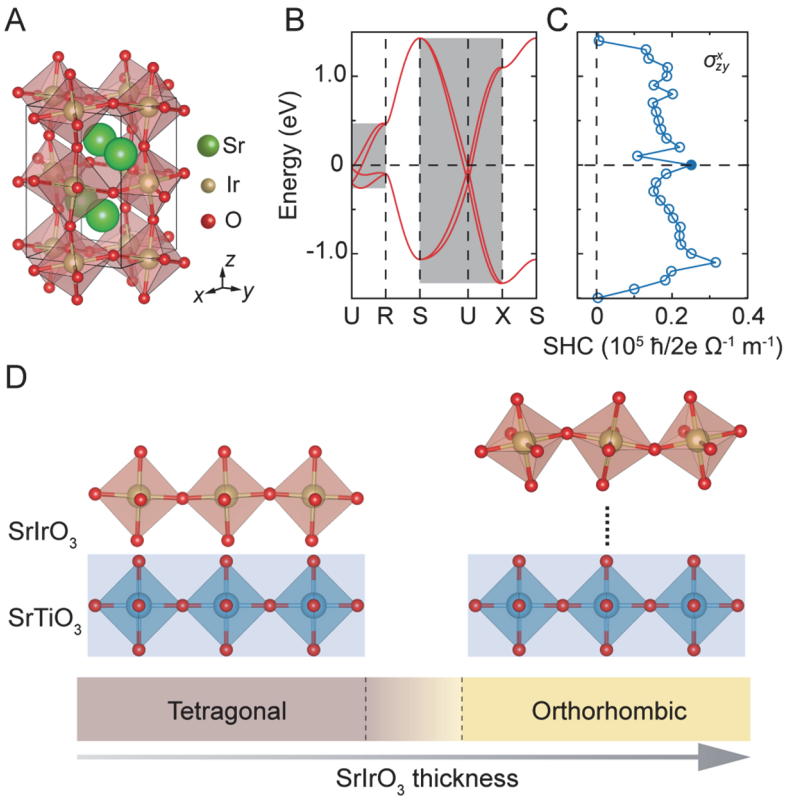

Fig. 1. The mechanism of the spin-Hall effect in $SrIrO_3$. (*A*) Orthorhombic perovskite crystal structure of bulk $SrIrO_3$, where *x*, *y*, and *z* correspond to the $[100]_o$, $[010]_o$, and $[001]_o$ directions, respectively. (*B*) Electron band structure of bulk $SrIrO_3$ along the path U-R-S-U-X-S of the Brillouin zone, where the gray boxes highlight the nearly degenerate energy bands responsible for the large bulk SHC. (*C*) Calculated bulk $SrIrO_3$ spin-Hall conductivity (SHC) σ^x_{zy}, where the charge current, spin current and spin polarization direction are along *y*, *z* and *x*, respectively. (*D*) Schematic illustrations of the lattice symmetry of $SrIrO_3$ when grown on cubic non-tilted $SrTiO_3$, where a partial suppression of the IrO_6 octahedral tilt exists up to a certain thickness before a tilted octahedral pattern is established in thicker films.

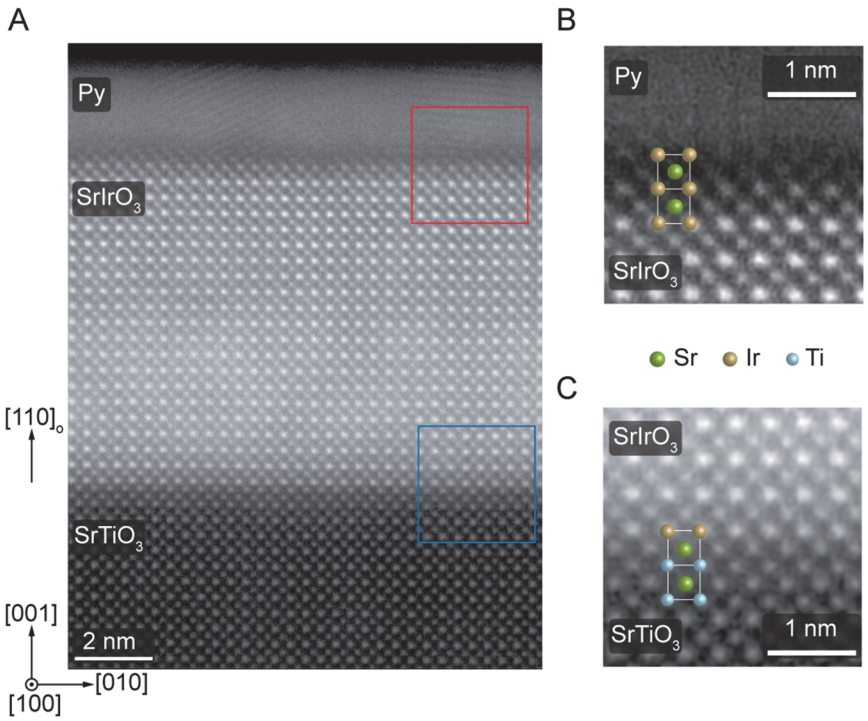

Fig. 2. The structural characterization of the Py/$SrIrO_3$/$SrTiO_3$ system. (*A*) Scanning transmission electron microscope image of Py/$SrIrO_3$ heterostructure on (001) $SrTiO_3$ substrate. The image contrast is approximately proportional to the atomic number *Z*, where brighter colors represent heavier elements. (*B,C*) Expanded image of the top Py/$SrIrO_3$ interface *B*, and the bottom $SrIrO_3$/$SrTiO_3$ interface *C*, showing the high quality $SrIrO_3$ film with atomically-sharp interfaces. The stacking of the atomic constituents is highlighted in the blown-up images by the superimposed filled dots of different colors (Sr in green, Ir in yellow and Ti in blue).

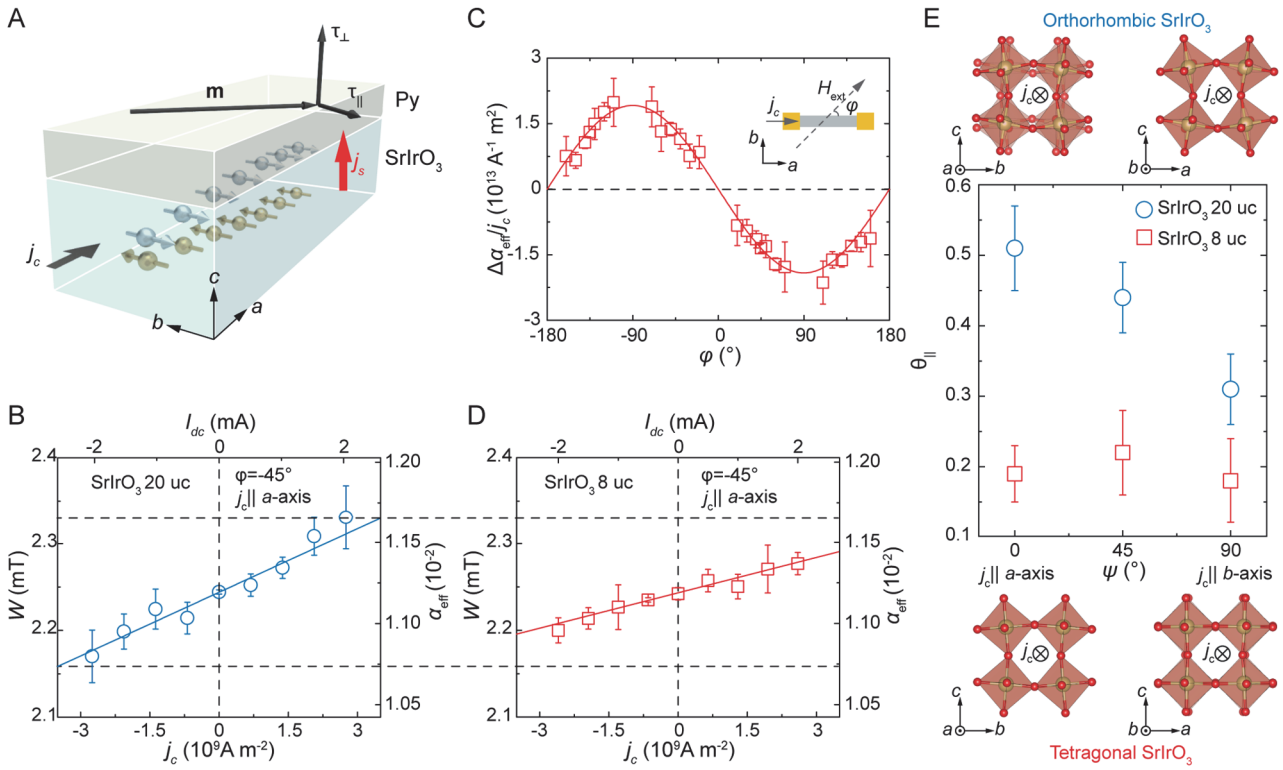

Fig. 3. ST-FMR measurements. (*A*) Schematic of the Py/$SrIrO_3$ bilayer on $SrTiO_3$(001) and the current-induced torque geometries. Incoming charge current (j_c) generates a spin current (j_s) along the out-of-plane $[110]_o$ direction or *c*-axis. The pseudocubic indices *a*, *b* and *c* correspond to orthorhombic $[1\bar{1}0]_o$, $[001]_o$ and $[110]_o$ directions, respectively. (*B*) Resonance linewidth *W* and effective magnetic damping α_{eff} as functions of dc charge current I_{dc} and current density j_c in $SrIrO_3$ for a 3.5 nm Py/8 nm (20 uc) $SrIrO_3$ microstripe (20 μm × 40 μm). The current is applied along the $[1\bar{1}0]_o$ direction (*a*-axis) and the external magnetic field is oriented at an angle φ=-45° with respect to the current axis. The applied microwave frequency and power are 5.5 GHz and 15 dBm, respectively. The solid line represents a linear fitting. (*C*) Current modulation of Py effective damping as a function of external magnetic field angle for the 3.5 nm Py/8 nm (20 uc) $SrIrO_3$ sample. The solid line shows the fit to sin(φ). Resonance linewidth *W* and effective magnetic damping α_{eff} as functions of dc current and current density. (*D*) Change of *W* and α_{eff} due to j_c in a 3.5 nm Py/3.2 nm (8 uc) $SrIrO_3$ sample. (*E*) In-plane crystallographic orientation dependence of the spin-torque ratio $\theta_{\parallel}$ for Py/$SrIrO_3$ bilayers (with Py thickness fixed at 3.5 nm) with two different $SrIrO_3$ film thicknesses. ψ is the angle between the $[1\bar{1}0]_o$ direction (*a*-axis) and the applied current axis. The top and bottom schematics illustrate the planar crystalline geometry of $SrIrO_3$ viewed along *a*- and *b*-axis for orthorhombic and tetragonal symmetries, respectively.

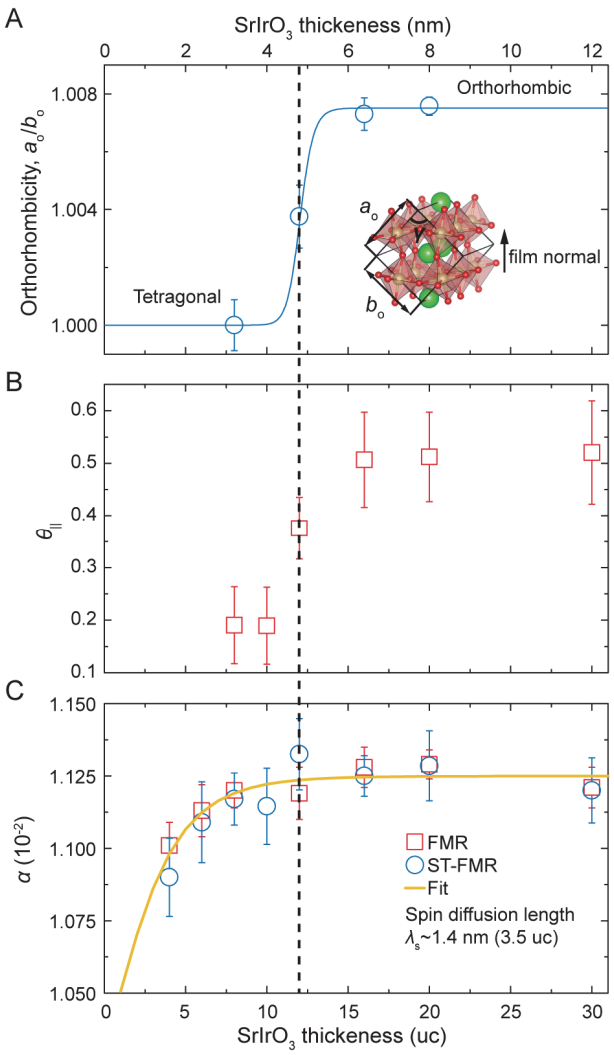

Fig. 4. Control of spin-torque ratio with lattice symmetry stabilization. (*A*) Thickness dependence of orthorhombicity factor, defined as a_o/b_o, of $SrIrO_3$ thin films. The solid line is a guide to illustrate the $SrIrO_3$ crystalline symmetry transition. Inset shows the schematic of the $SrIrO_3$ orthorhombic unit cell with the tilted IrO_6 octahedra, where the arrow indicates the thin film growth direction (*c*-axis or $[110]_o$). γ is the angle between a_o- and b_o-axis. (*B*) $SrIrO_3$ thickness dependence of spin orbit ratio $\theta_{\|}$ for Py/$SrIrO_3$ bilayers (with Py thickness fixed at 3.5 nm). (*C*) $SrIrO_3$ thickness dependence of Gilbert damping parameter α determined by the broadband FMR (red) and ST-FMR (blue) measurements for Py/$SrIrO_3$ bilayers (with Py thickness fixed at 3.5 nm). The solid line represents the fit to the diffusive spin-pumping model, which gives a spin-diffusion length λ_s ~1.4 nm for $SrIrO_3$.